Coupling of Ca^{2+} and voltage activation in BK channels through the αB helix/voltage sensor interface

Yanyan Geng[a], Zengqin Deng[b], Guohui Zhang[c], Gonzalo Budelli[d,1], Alice Butler[d], Peng Yuan[b], Jianmin Cui[c], Lawrence Salkoff[d,e], and Karl L. Magleby[a,2]

[a]Department of Physiology and Biophysics, University of Miami Miller School of Medicine, Miami FL 33136; [b]Department of Cell Biology and Physiology, Washington University, St. Louis, MO 63110; [c]Department of Biomedical Engineering, Washington University, St. Louis, MO 63110; [d]Department of Neuroscience, Washington University, St. Louis, MO 63110; and [e]Department of Genetics, Washington University, St. Louis, MO 63110

Edited by Christopher J. Lingle, Washington University Medical Center, St. Louis, MO, and accepted by Editorial Board Member David E. Clapham April 23, 2020 (received for review May 13, 2019)

Large-conductance Ca^{2+} and voltage-activated K^+ (BK) channels control membrane excitability in many cell types. BK channels are tetrameric. Each subunit is composed of a voltage sensor domain (VSD), a central pore-gate domain, and a large cytoplasmic domain (CTD) that contains the Ca^{2+} sensors. While it is known that BK channels are activated by voltage and Ca^{2+}, and that voltage and Ca^{2+} activations interact, less is known about the mechanisms involved. We explore here these mechanisms by examining the gating contribution of an interface formed between the VSDs and the αB helices located at the top of the CTDs. Proline mutations in the αB helix greatly decreased voltage activation while having negligible effects on gating currents. Analysis with the Horrigan, Cui, and Aldrich model indicated a decreased coupling between voltage sensors and pore gate. Proline mutations decreased Ca^{2+} activation for both Ca^{2+} bowl and RCK1 Ca^{2+} sites, suggesting that both high-affinity Ca^{2+} sites transduce their effect, at least in part, through the αB helix. Mg^{2+} activation also decreased. The crystal structure of the CTD with proline mutation L390P showed a flattening of the first helical turn in the αB helix compared to wild type, without other notable differences in the CTD, indicating that structural changes from the mutation were confined to the αB helix. These findings indicate that an intact αB helix/VSD interface is required for effective coupling of Ca^{2+} binding and voltage depolarization to pore opening and that shared Ca^{2+} and voltage transduction pathways involving the αB helix may be involved.

Slo1 channel | BK channel | Ca^{2+}-activated K^+ channel | allosteric coupling | patch clamp

Large-conductance Ca^{2+}- and voltage-activated K^+ channels (BK, Slo1, Maxi-K, $K_{Ca}1.1$, *KCNMA1* gene) are widely distributed and opened by the synergistic action of depolarization and intracellular Ca^{2+} (1–19) with intracellular Mg^{2+} modulating the activation (20, 21). Open BK channels allow the outward movement of intracellular K^+, which drives the membrane potential in a negative direction, decreasing the excitability of cells by deactivating voltage-dependent Na^+ and Ca^{2+} channels. Through this negative feedback system, BK channels modulate many physiological processes, including smooth muscle contraction (22), release of neural transmitters (23), repetitive firing in neurons (24), and renal K^+ secretion (25). Defects in BK channels can lead to epilepsy, dyskinesia (26, 27), and hypertension (25) and contribute to human obesity (28). The voltage- and Ca^{2+}-dependent gating of BK channels can be described by two-tiered allosteric gating mechanisms formulated as discrete state models (5, 12) and also by more general models (6), including the modulation by Mg^{2+} (20, 29, 30). However, less is understood about the specific allosteric pathways involved in voltage and Ca^{2+} activation of the channel.

It is known that the BK channel is of modular design, with the voltage sensors and pore gate forming the transmembrane domain of the channel (TMD) and the large cytoplasmic domain (CTD) containing the Ca^{2+} sensors (3, 4, 7–9, 11–18). Removing the CTD removes all Ca^{2+} sensitivity (31), leaving a voltage-gated channel (31, 32). However, the coupling between voltage sensors and the pore gate is greatly reduced in the absence of the CTD (32), leading to a marked decrease in voltage activation (31, 32). This suggests that the CTD may also contribute to transduction from voltage sensors to the pore gate. Previous studies have identified a dynamic interface between the αB helix of the CTD and the voltage sensors (17, 18, 33). The purpose of our paper is to determine the contributions of the αB helix at this interface to voltage and Ca^{2+} activation.

The structure of one of the four identical subunits of a BK channel is shown by the cartoon in Fig. 1*A*, and the complete cryogenic electron microscopy (cryo-EM) structures of metal-free and Ca^{2+}- and Mg^{2+}-bound human BK channels are shown in Fig. 1 *C* and *D* (19). Each subunit has a voltage sensor domain (VSD) composed of transmembrane segments S1 to S4 that are preceded by an S0 transmembrane segment that modulates the voltage sensor (34). Following S4 are transmembrane segments S5 and S6, which contribute to the central pore-gate domain (PGD), which is formed from four such S5 and S6 pairs, one from each subunit. The location of the gate that blocks the

Significance

Large-conductance BK (Slo1) K^+ channels are activated by voltage, Ca^{2+}, and Mg^{2+} to modulate membrane excitability in neurons, muscle, and other cells. BK channels are of modular design with pore-gate and voltage sensors as transmembrane domains and a large cytoplasmic domain (CTD) containing the Ca^{2+} sensors. Previous observations suggest that voltage and Ca^{2+} sensors interact, but less is known about this interaction and its involvement in the gating process. We show that a previously identified structural interface between the CTD and voltage sensors is required for effective activation by both voltage and Ca^{2+}, suggesting that these processes may share common allosteric activation pathways. Such knowledge should help explain disease processes associated with BK channel dysfunction.

Author contributions: Y.G., Z.D., G.Z., G.B., A.B., P.Y., J.C., L.S., and K.L.M. designed research; Y.G., Z.D., G.Z., G.B., A.B., P.Y., J.C., L.S., and K.L.M. performed research; Y.G., Z.D., G.Z., G.B., A.B., P.Y., J.C., L.S., and K.L.M. analyzed data; and Y.G., Z.D., G.Z., A.B., P.Y., J.C., L.S., and K.L.M. wrote the paper.

The authors declare no competing interest.

This article is a PNAS Direct Submission. C.J.L. is a guest editor invited by the Editorial Board.

Data deposition: Data have been deposited in the Protein Data Bank, https://www.wwpdb.org/, for the human BK L390P mutant under PDB ID 6V5A.

[1]Present address: Department of Biology, Brandeis University, Waltham, MA 02453.

[2]To whom correspondence may be addressed. Email: kmagleby@miami.edu.

This article contains supporting information online at https://www.pnas.org/lookup/suppl/doi:10.1073/pnas.1908183117/-/DCSupplemental.

First published June 8, 2020.

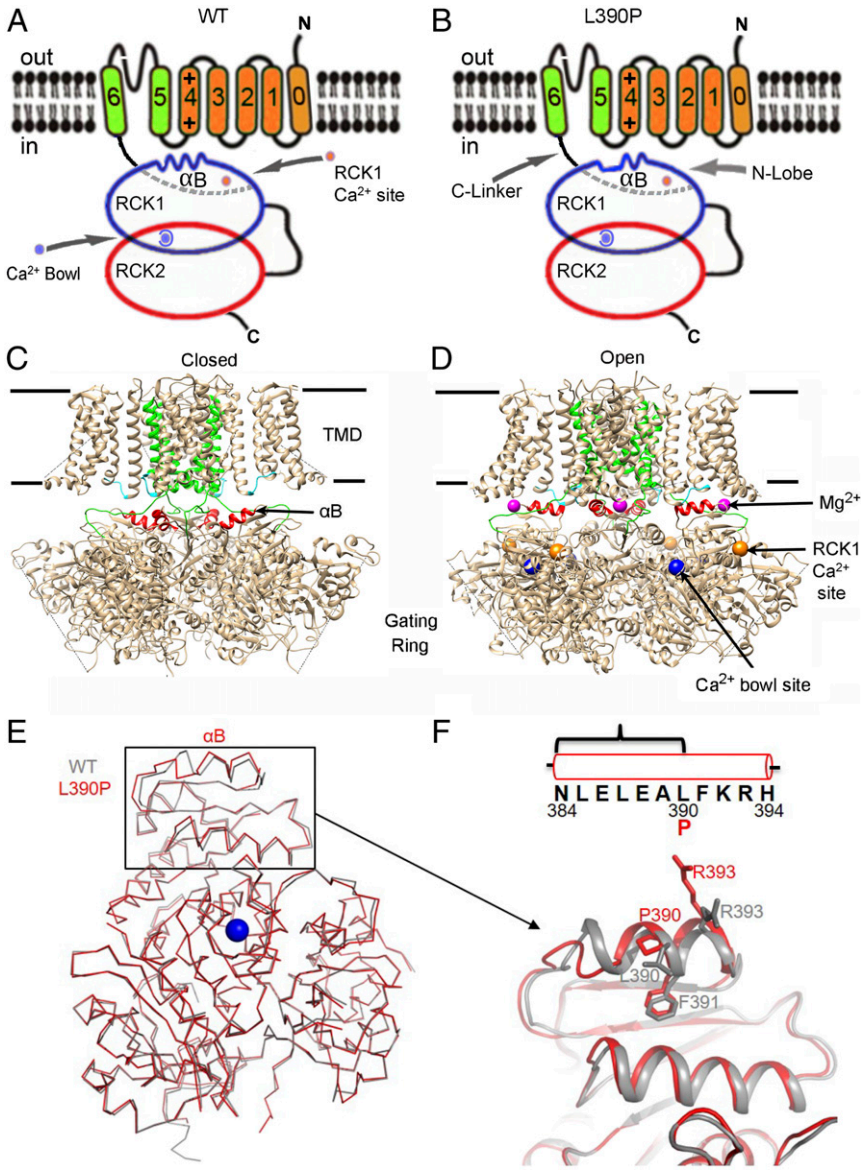

Fig. 1. Cartoon, cryo-EM structures, and crystal structures of specified parts of the BK channel. (*A* and *B*) Cartoon of one subunit of the tetrameric BK channel modified from ref. 55, with permission from AAAS. In the channel the αB helix is under the S4–S5 linker/VSD of an adjacent subunit in a swapped manner. S1 to S4 form the voltage sensor, S5 and S6 contribute to the pore-gate domain, and a C-linker connects S6 to the N-lobe of the RCK1 domain. Ca^{2+} bowl and RCK1 Ca^{2+} sites are shown. The αB helix of the N-lobe interacts with the S4–S5 linker and voltage sensor from an adjacent subunit in a swapped configuration (17). L390P disrupts the first turn of the αB helix, which would reduce the effectiveness of the αB helix/S4–S5 linker voltage sensor interface. (*C*) The cryo-EM structure of the human BK channel in the ethylenediaminetetraacetic acid (EDTA) Ca^{2+}- and Mg^{2+}-free, presumably closed, state (PDB ID 6V3G) (19), and (*D*) in the Ca^{2+}- and Mg^{2+}-bound, presumably open, state (PDB ID 6V38) (19). S0 to S4, which include the voltage sensor, are in silver; S5 and S6 are in green; and the S4–S5 linkers are in cyan. The αB helices (red) forming the top of the RCK1 N-lobes move upward and outward from closed to open, where they could push upward and outward on the S4–S5 linkers and voltage sensor domains. Ca^{2+} and Mg^{2+} sites are indicated as colored balls. (*E* and *F*) The proline substitution L390P of the αB helix caused local perturbations limited to flattening the first turn of the αB helix. (*E*) Superposition of crystal structures of WT human BK CTD in gray (PDB ID 3MT5) (55) and the L390P mutant CTD structure determined in this paper in red (PDB ID 6V5A). The most N-terminal residue is K343. Refinement details are in *SI Appendix*, Table S1. (*F*) A close-up view shows that the L390P mutation flattens the first turn of the αB helix (WT in gray, mutant in red). A schematic of the residues in the αB helix is above the structure of the helix. The bracket indicates the altered structure with first residue N384 and ends with the different side chain of L390P.

central pore is debated, but movement of the pore-lining segment S6 in the intracellular cavity near the entrance to the selectivity filter may reposition hydrophobic residues to exclude water, blocking conduction (35, 36). The four VSDs surround the central pore-gate domain.

The large CTD of the BK channel, also referred to as the gating ring (10, 33), is seen below the TMD in Fig. 1 *C* and *D*). Each subunit contributes tandem RCK1 and RCK2 domains to the CTD, for a total of eight RCK domains. Each RCK1 contains a high-affinity RCK1 Ca^{2+}-binding site (7, 37), and each RCK2 contains a high-affinity Ca^{2+} bowl-binding site (4), for a total of eight high-affinity Ca^{2+} sites in the CTD. In addition, there are four low-affinity Mg^{2+} sites per channel, each coordinated between residues on the top of the CTD and the bottom of the voltage sensor (30). Removing the CTD removes all Ca^{2+} and Mg^{2+} sensitivity (31).

The CTD is anchored to the TMD through four peptide C-linkers, each connecting S6 of the TMD to the N-lobe of the

RCK1 domain of the same subunit in a swapped manner. BK channels have a relatively short S4–S5 linker extending from S4 in the VSD to S5 in the PGD of the same subunit. The short S4–S5 linker in BK would constrain the depolarization-induced upward movement of S4 in BK (17, 18), which may explain why only one positive residue in each S4 contributes to the voltage dependence of gating in BK (38).

Ca^{2+} binding to the Ca^{2+} bowl and RCK1 sites in the CTD leads to a near rigid-body lateral tilting (away from pore) of the N-lobes formed by the upper part of each RCK1 domain (17, 18, 33). This lateral tilting moves the RCK1 attachment point for each S6-RCK1 C-linker laterally and downward, pulling on S6 to potentially open the pore gate. Simultaneously, the lateral tilting of the N-lobe moves the αB helix located at the top of each N-lobe both upward and laterally to push upward and laterally on the bottom of the S4–S5 linker/VSD to potentially open the channel (17, 18). A morphing movie in Hite et al. (18) clearly illustrates these simultaneous actions of the Ca^{2+}-induced pulling on S6 through the C-linker and the upward and lateral pushing on the S4–S5 linker/VSD. A similar upward and outward movement of the αB helices at the top of the N-lobes induced by 10 mM Ca^{2+} for human BK channels can be seen in a movie in Yuan et al. (33) and in *SI Appendix*, Fig. S1. Supporting the fact that Ca^{2+}-induced pulling on the S6-RCK1 linkers contributes to channel opening are the observations that shortening the C-linkers by deleting amino acids increases open probability over a range of Ca^{2+} concentrations and that lengthening the C-linkers decreases open probability (39, 40).

In the absence of Ca^{2+}, shortening the C-linkers left shifts $V_{1/2}$, the voltage for half activation, to more negative potentials, and lengthening the C-linkers right shifts $V_{1/2}$ to more positive potentials (40). These shifts in voltage activation induced by changing the length of the C-linker arising from the Ca^{2+}-sensing CTD suggests coupling between the Ca^{2+} and voltage activation pathways. This observation is one of many suggesting coupling between voltage and Ca^{2+} activation in BK channels, as detailed in reviews (15, 16, 41). A few of these observations will be mentioned. Removing the CTD right shifts $V_{1/2}$ by >50 mV (31) by decreasing the coupling between voltage sensor movement and the pore gate (32). A small but significant interaction between Ca^{2+} binding and voltage sensor activation is required to account for the Ca^{2+} dependence of Po (6). Ca^{2+} binding to the RCK1 Ca^{2+} site is voltage dependent (42). Functional studies suggest that residues in the AC region (N-lobe) of the CTD interact with the VSD (27). Ca^{2+} binding alters VSD rearrangement (43). Ca^{2+} sensor occupancy left shifts the Q-V curves with strong allosteric coupling between Ca^{2+}-binding sites and voltage sensors (44). Strong correlations have been observed between VSD rearrangements and conformational changes in the CTD, which support a pathway that couples Ca^{2+} binding to channel opening through the voltage sensor (45). Mg^{2+} binding between the VSD and the CTD directly couples voltage, Ca^{2+}, and Mg^{2+} sensors (21, 30).

The structural studies (17, 18) discussed above, and Fig. 1 *C* and *D* and *SI Appendix*, Fig. S1, showing that the αB helices at the top of the N-lobe of the CTD interact directly with the S4–S5 linker/VSD, implicate the αB helix as a potential key structural element in the coupling between voltage and Ca^{2+} sensors and suggest that the αB helix may be part of a shared pathway for voltage and Ca^{2+} activation (18). Functional support for this proposal is the finding from an alanine scan of the AC region of the N-lobe that alanine substitution at two sites in the αB helix decreased both Ca^{2+} sensitivity (27) and interactions among residues in the αB helix and VSD (21). A prediction of coupling of voltage and Ca^{2+} sensors through the αB helix is that disruption of the αB helix should alter both Ca^{2+} and voltage activation of the BK channel.

In this paper we test this hypothesis by disrupting the αB helix with point proline mutations. We first examined a proline substitution in the middle of the helix and found that L390P shifted voltage activation to more positive potentials and decreased Ca^{2+} sensitivity. A high-resolution crystal structure of the CTD L390P mutant showed that the effects of the mutation were localized to the αB helix, limited to flattening one turn of the αB helix. L390P did not alter the normalized gating currents. Fitting of Po versus voltage data with the Horrigan, Cui, and Aldrich (HCA) model (46) indicated that L390P reduced voltage activation by decreasing the coupling between voltage sensors and the pore gate. Mutations eliminating either the high-affinity RCK1 Ca^{2+} sites or the Ca^{2+} bowl sites showed that L390P still reduced Ca^{2+} activation when either type of site was examined separately, suggesting that both types of high-affinity Ca^{2+} sites require an intact αB helix for full function. Proline mutations at other sites in the αB helix also reduced both voltage and Ca^{2+} activation. αB helix mutations also decreased activation by 10 mM Mg^{2+} acting at the low-affinity Mg^{2+} site. Our findings suggest that an intact αB helix is required for effective voltage, Ca^{2+}, and Mg^{2+} activation of BK channels. Coupling of voltage, Ca^{2+}, and Mg^{2+} activation through the αB helix would allow voltage, Ca^{2+}, and Mg^{2+} to share activation pathways.

Results

Disruption of the αB Helix Right Shifts $V_{1/2}$ to More Positive Potentials. If the αB helix plays a major role in the transduction of voltage and Ca^{2+} activation to the pore gate in BK channels, then disruption of the αB helix might be expected to alter voltage and Ca^{2+} activation of the channel. To test this hypothesis, a proline was substituted for a leucine in the middle of the three-turn αB helix that interfaces with the S4–S5 linker/VSD to obtain L390P channels (Fig. 1 *A* and *B*). X-ray crystallography then indicated that the L390P mutation caused a structural change to the αB helix by flattening the first turn of the helix, with structural changes limited to the αB helix (Fig. 1 *B*, *E*, and *F*).

To test if these structural changes to the αB helix altered voltage and Ca^{2+} activation, the voltage required for half-activation of the channel, $V_{1/2}$, was determined for L390P channels for comparison to wild-type (WT) channels. $V_{1/2}$ for WT and L390P channels was first obtained in the absence of Ca^{2+} to determine the effect of αB helix disruption on voltage activation. $V_{1/2}$ was then determined in the presence of 100 μM Ca^{2+} to measure the effect of αB helix disruption on Ca^{2+} activation.

For WT channels in 0 μM Ca^{2+}, the mean voltage for half-activation was 176 mV (SEMs and *P* values are in *SI Appendix*, Table S2). Disruption of the αB helix with L390P then right-shifted the G-V curve to more positive potentials, giving a mean $V_{1/2}$ of 242 mV. This indicated that a 66-mV greater depolarization was required to activate the channel in the absence of Ca^{2+} after disrupting the αB helix (Fig. 2 and *SI Appendix*, Fig. S2 and Table S2). Proline substitutions at other positions along the αB helix (L385P, L387P, E388P, A389P, F391P, and F394P) also right-shifted the voltage required for half-activation in the absence of Ca^{2+} from 44 to 109 mV, depending on the location of the mutation (Fig. 2 and *SI Appendix*, Fig. S2 and Table S2). Hence, more positive potentials are required to activate the channel when the αB helix is disrupted, indicating that an intact αB helix is required for effective voltage activation.

Quantifying the Protein Interaction Interface between the αB Helix and the S4–S5 Linker/VSD. Fig. 1 shows that the structural changes from mutating the αB helix with L390P were localized to the αB helix (Fig. 1 *E* and *F*). Consequently, for the mutated αB helix to alter gating, the mutation would have to alter functional interaction at an interface between the αB helix and some other part of the channel. Hite et al. (18) have identified a protein–protein

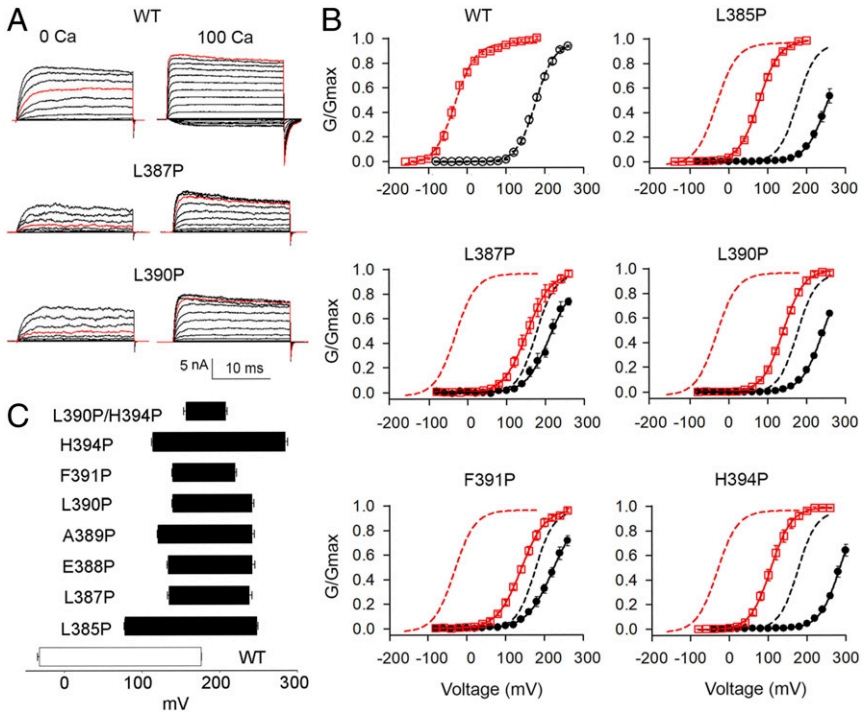

Fig. 2. Proline mutations of the αB helix decrease both voltage and Ca^{2+} activation. (*A*) Current recordings from the indicated channels using inside-out macro patches. Voltage pulses were from −80 to 260 mV with 20-mV increments, except for WT 100 μM Ca^{2+}, which were from −160 to 180 mV. Red trace for WT 100 μM Ca^{2+} is current at 180 mV. Other red traces are currents at 200 mV. (*B*) G/G_{max} vs. V plots in 0 Ca^{2+} (black lines through black filled circles; $n \geq 4$) and 100 μM Ca^{2+} (red lines through red open squares; $n \geq 4$). Dashed lines are Boltzmann fits for WT channels and continuous lines for mutated channels. Additional data are in *SI Appendix*, Fig. S2. Boltzmann fit parameters, SEMs, and *P* values are in *SI Appendix*, Table S2. (*C*) $V_{1/2}$-Ca^{2+} bar plots, where the right end of each bar indicates 0 μM Ca^{2+} and the left end 100 μM Ca^{2+} as mean and SEM. Bar length is taken as a measure of Ca^{2+} sensitivity.

interface between the RCK1 N-lobe and the S4–S5 linker/VSD in open *Aplysia* BK channels. To quantify this interface in a vertebrate BK channel, we measured the protein interaction interface (buried surface area), which is a direct measurement of protein–protein interaction, between the αB helix and the S4–S5 linker/VSD for both Ca^{2+}-free closed and Ca^{2+}-bound open channels using human BK channel structures from ref. 19. For Ca^{2+}-free closed channels, the area per subunit of the protein interaction interface between the αB helix and the S4–S5 linker was 117 $Å^2$, with no interaction of the αB helix with the VSD (*SI Appendix*, Fig. S1*A*). For Ca^{2+}-bound open channels, the interface area per subunit between the αB helix and S4–S5 linker increased threefold to 360 $Å^2$, and the αB helix also then interfaced with the VSD, giving a combined interface area of the αB helix with the S4–S5 linker/VSD of 724 $Å^2$ per subunit in open channels (*SI Appendix*, Fig. S1*B*).

Our observations that the L390P mutation flattens the first turn of the αB helix at the interface with the S4–S5 linker/VSD, with no significant changes in structure elsewhere in the RCK1-RCK2 domains, including the αA helix, the αC helix, and the attachment point of the C-linker to the RCK1 domain (Fig. 1 *E* and *F*), suggest that the L390P mutation alters gating by altering the interface between the αB helix and the S4–S5 linker/VSD. That both Ca^{2+} and voltage activation are reduced by L390P acting at this interface suggests that this interface could provide a common pathway through which voltage and Ca^{2+} activation could interact.

Disruption of the αB Helix with L390P Has Negligible Effect on Gating Charge Movement. In contrast to the large right shifts in $V_{1/2}$ required for activation with proline substitution in the αB helix, the voltage sensitivity of activation, as indicated by the slopes of the G-V curves, remained relatively unchanged (Fig. 2 and *SI Appendix*, Fig. S2 and Table S2). Similar slopes suggest similar effective charge movement for activation.

If effective charge movement is similar after disruption of the αB helix, what then accounts for the large right shifts in $V_{1/2}$? One possibility is that the movement of the voltage sensors occurs at right-shifted voltages after disrupting the αB helix. Another is that pore opening is no longer tightly coupled to voltage sensor movement (32). A comparison of gating currents recorded from WT and L390P channels indicated that disruption of the αB helices had negligible effect on Q-V curves (Fig. 3). Hence,

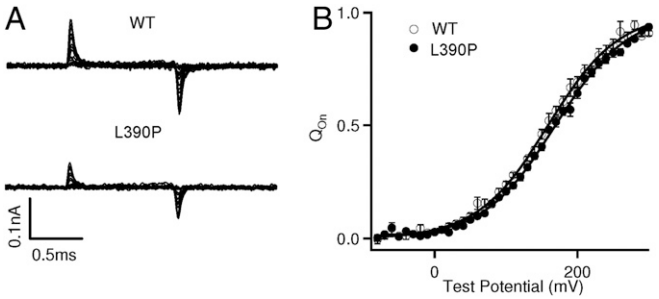

Fig. 3. Disrupting the αB helix with L390P has negligible effect on the gating current. (*A*) Gating currents of WT and L390P BK channels. Voltage pulses were from −30 to 300 mV (WT) or from −80 to 300 mV (L390P) with 20-mV increments. (*B*) Normalized gating charge-voltage (Q-V) curves for on-gating currents. The smooth curves are fits to the Boltzmann function with a $V_{1/2}$ and slope factor of 159.1 ± 6.5 mV and 49.0 ± 6.7 mV for WT and 169.0 ± 6.7 mV and 50.7 ± 5.1 mV for L390P. The data points represent the mean ± SEM; $n = 8$ for WT and $n = 10$ for L390P.

the right shift in the G-V curves with L390P does not arise from a right shift in voltage sensor activation.

Disruption of the αB Helix with L390P Increases the Intrinsic C-O Equilibrium Constant L_0 and Decreases the Coupling Factor D between Voltage Sensors and Pore Gate. We next considered whether the L390P-induced right shift in G-V curves arose from a decrease in the intrinsic closed–open equilibrium constant L_0 or from a decrease in the allosteric factor D that couples voltage sensor activation to pore gate opening (32, 46). Po was measured over wide ranges of voltage for WT and L390P channels with 0 μM intracellular Ca^{2+}. Compared to WT, L390P increased Po at negative potentials (Fig. 4 *B* and *C*) and decreased Po at positive potentials (Fig. 4*C*). Fitting the Po versus V curves with the HCA model (46) indicated that L390P increased L_0 12.8-fold, from $7.42 \times 10^{-7} \pm 0.96 \times 10^{-7}$ for WT channels to $9.47 \times 10^{-6} \pm 2.17 \times 10^{-6}$ for L390P channels ($P < 0.01$), and decreased D by 4.94-fold, from 29.3 ± 3.0 for WT channels to 5.93 ± 0.73 for L390P channels ($P < 0.0001$). The L390P-induced increase in L_0 and decrease in D had differential effects on Po depending on the membrane potential because D is applied at increasing power with each activated voltage sensor (Fig. 4*A*). At very negative potentials with no activated voltage sensors, D has no effect, so that the L390P-induced increase in L_0 dominates, increasing Po. At very positive potentials with four activated voltage sensors, the L390P-induced reduction in D decreases effective coupling 596-fold ($29.3^4_{WT}/5.93^4_{L390P}$), leading to a reduced Po compared to WT. To activate the channel with L390P then requires more depolarization leading to the right shifts in the GV curves at positive potentials (Fig. 2). The increased L_0 suggests that disruption of the αB helix removes a normal inhibition on opening in WT channels at negative potentials. Similar to the dual action of the L390P mutation on increasing L_0 and decreasing D, removing the entire gating ring also removes a normal inhibition on opening and decreases coupling between voltage sensors and pore gate (32).

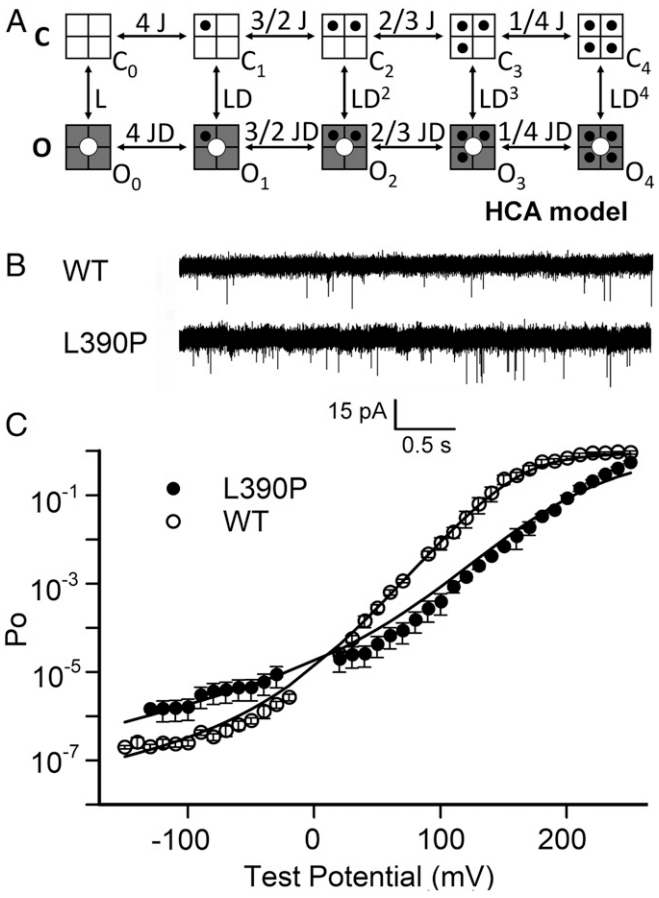

Fig. 4. L390P increases the intrinsic closed-open equilibrium and decreases the coupling between voltage sensors and pore gate. (*A*) HCA model (46) for voltage-dependent gating of BK channels. *L* is the closed-to-open equilibrium constant for pore opening. *D* is the allosteric factor coupling voltage sensor activation to channel opening. *J* is the relaxed to activated equilibrium constant for each voltage sensor when the pore gate is closed. Channel opening increases *D*-fold for each activated voltage sensor (black dot). *L* and *J* increase with depolarization. (*B*) Single-channel currents recorded at −120 mV from membrane patches containing many channels. (*C*) Plot of Po versus voltage for WT and L390P channels. WT data from Zhang et al. (32). Data were obtained with 0 μM intracellular Ca^{2+}. The continuous lines are fits with the HCA (46) model with parameters for WT: L_0 = 7.42E-7, D = 29.3, Z_J = 0.520 e_o, Z_L = 0.341 e_o, Vhc = 159 mV; and for L390P: L_0 = 9.47E-6, D = 5.94, Z_J = 0.503 e_o, Z_L = 0.440 e_o, Vhc = 169 mV, where L_0 is L at 0 mV. $n \geq 4$.

Disruption of the αB Helix Decreases High-Affinity Ca^{2+} Sensitivity. Removing the CTD (31) or mutating both the RCK1 and calcium bowl Ca^{2+}-binding sites in the CTD (7, 8) removes all Ca^{2+} sensitivity from BK channels. Hence, the CTD is necessary both to bind Ca^{2+} and to transfer the energy of Ca^{2+} binding in the CTD to the PGD to open the channel. If the αB helix is involved in this transduction, then disruption of the αB helix might be expected to reduce Ca^{2+} sensitivity. This question was explored by using the Ca^{2+}-induced leftward shift in $V_{1/2}$ as a measure of Ca^{2+} sensitivity (47). For WT BK channels, increasing Ca^{2+} from 0 to 100 μM left-shifted $V_{1/2}$ from 176 to −32 mV, for a Δ shift of −208 mV (Fig. 2 and *SI Appendix*, Table S2, which includes SEMs and *P* values). Thus, for WT channels, 0 to 100 μM Ca^{2+} provided activation equivalent to Δ208 mV of depolarization, as the voltage had to be shifted Δ−208 mV to negate the opening effect of 100 μM Ca^{2+}.

In contrast, after disrupting the αB helix with L390P, increasing Ca^{2+} from 0 to 100 μM left-shifted $V_{1/2}$ from 242 to 140 mV, for a Δ shift of −102 mV, only 49% of the Δ−208 mV Ca^{2+}-induced left shift for WT (Fig. 2 and *SI Appendix*, Table S2). Thus, disrupting the αB helix with L390P reduced the effective transduction of high-affinity Ca^{2+} binding from the gating ring to the pore gate by 51%.

Proline substitutions at positions L385P, L387P, E388P, A389P, F391P, and H394P in the αB helix also reduced the Ca^{2+}-induced left shift in $V_{1/2}$, with reductions to 82, 50, 52, 58, 38, and 82% of WT, respectively (Fig. 2 and *SI Appendix*, Fig. S2 and Table S2). L387P and F391P gave the greatest reduction in Ca^{2+} sensitivity, consistent with previous observations obtained from an alanine scan of the αB helix, where L387A and F391A were found to reduce Ca^{2+} sensitivity (27). The reduction in Ca^{2+} sensitivity by L387A and F391A was less than half the reduction with proline substitutions at these sites, indicating that side-chain replacement with alanine can also reduce Ca^{2+} sensitivity, but that disrupting the αB helix with proline is more effective. Taken together, the observations in this section indicate that an intact αB helix is required to fully couple Ca^{2+} binding in the CTD to pore opening in the PGD.

Interestingly, the proline mutations L385P and H394P near the ends of the αB helix gave the smallest reductions in Ca^{2+} sensitivity, but the greatest right shifts of $V_{1/2}$ for voltage activation (Fig. 2 and *SI Appendix*, Fig. S2 and Table S2), indicating differential effects of the αB helix on Ca^{2+} and voltage activation, depending on the position of the substituted residues.

Disruption of the αB Helix Reduces High-Affinity Ca^{2+} Sensitivity through Both the Ca^{2+} Bowl and RCK1 Ca^{2+} Site. The previous section showed that disrupting the αB helix with L390P and other

proline mutations reduced Ca^{2+} activation. To examine whether this reduction arose from decreased effectiveness of one or both high-affinity Ca^{2+} sensor pathways, we tested the effect of disrupting the αB helix on each Ca^{2+} sensor separately. The mutation D898-902N (5D5N) (4, 7) was used to eliminate the Ca^{2+} bowl, leaving only the RCK1 Ca^{2+} sensor pathway, and the mutation D362A/D367A (2D2A) (7) was used to eliminate the RCK1 Ca^{2+} site, leaving only the Ca^{2+} bowl sensor pathway.

$\Delta V_{1/2\ 0\rightarrow 100\ \mu M\ Ca}$ was −208 mV for WT channels, −166 mV for 5D5N channels, and −54 mV for L390P/5D5N channels (Fig. 5 and *SI Appendix*, Fig. S3 and Table S3, which includes SEMs and *P* values). Removing the Ca^{2+} bowls thus reduced Ca^{2+} sensitivity to 80% of WT, indicating that RCK1 Ca^{2+} sites in the absence of Ca^{2+} bowls can contribute 80% of the total Ca^{2+} sensitivity of WT channels. Disrupting the αB helix of these 5D5N channels with L390P (L390P/5D5N channels) then reduced Ca^{2+} sensitivity to 33% of 5D5N channels (Fig. 5 and *SI Appendix*, Fig. S3 and Table S3).

$\Delta V_{1/2\ 0\rightarrow 100\ \mu M\ Ca}$ was −208 mV for WT channels, −119 mV for 2D2A channels, and −64 mV for L390P/2D2A channels. Removing the RCK1 Ca^{2+} sites thus reduced Ca^{2+} sensitivity to 57% of WT, indicating that the Ca^{2+} bowls in the absence of RCK1 sites can contribute 57% of the total Ca^{2+} sensitivity of WT channels. Disrupting the αB helix of these 2D2A channels with L390P (L390P/2D2A channels) then reduced the Ca^{2+} sensitivity to 54% of 2D2A channels. Thus, both types of high-affinity Ca^{2+} sites, Ca^{2+} bowl and RCK1, require an intact αB helix for their Ca^{2+} activation to be fully functional. However, L390P had differential effects on reducing the Ca^{2+} sensitivity from the two Ca^{2+} sites. L390P/5D5N channels had 33% of the Ca^{2+} sensitivity of 5D5N channels, whereas L390P/2D2A channels had 54% of the Ca^{2+} sensitivity of 2D2A channels (Fig. 5 and *SI Appendix*, Fig. S3 and Table S3).

In the absence of L390P mutations, our observations that RCK1 Ca^{2+} sites acting alone make a greater contribution to Ca^{2+} activation than Ca^{2+} bowl sites acting alone, and that the sum of $\Delta V_{1/2\ 0\rightarrow 100\ \mu M\ Ca}$ for RCK1 Ca^{2+} sites alone and Ca^{2+} bowl sites alone can exceed $\Delta V_{1/2\ 0\rightarrow 100\ \mu M\ Ca}$ for WT channels, has been described previously (48, 49). Also observed by others have been equal contributions of the RCK1 Ca^{2+} site and Ca^{2+} bowl to left shifts in $V_{1/2}$ (7, 8, 50) and equal contributions of these sites to decreasing the free energy necessary to activate voltage sensors (44). The reason for the apparent differences in the relative contributions from the two types of Ca^{2+} sites is not known.

Disruption of the αB Helix Reduces Low-Affinity Mg^{2+} Activation. The previous sections showed that disruption of the αB helix reduced high-affinity Ca^{2+} activation through both Ca^{2+} bowl and RCK1 Ca^{2+} sites. To explore whether proline mutations of the αB helix also changed activation through the low-affinity Mg^{2+} site, we compared the shift in $V_{1/2}$ for mutated and WT channels for 0 → 10 mM Mg^{2+}. In these experiments, Mg^{2+} would be expected to act predominantly on the low-affinity Mg^{2+} sites (29). Results for Mg^{2+} activation of WT channels and for seven different proline substitutions in the αB helix are presented (Fig. 6 and *SI Appendix*, Fig. S4 and Table S4, which includes SEMs and *P* values). For WT channels, $\Delta V_{1/2\ 0\rightarrow 10\ mM\ Mg}$ was −60 mV, generally consistent with previous work (7, 20, 29, 51). Proline mutations in the αB helix then reduced the Mg^{2+}-induced left shift to 57 to 92% of WT. Hence, an intact αB helix is required for full Mg^{2+} activation.

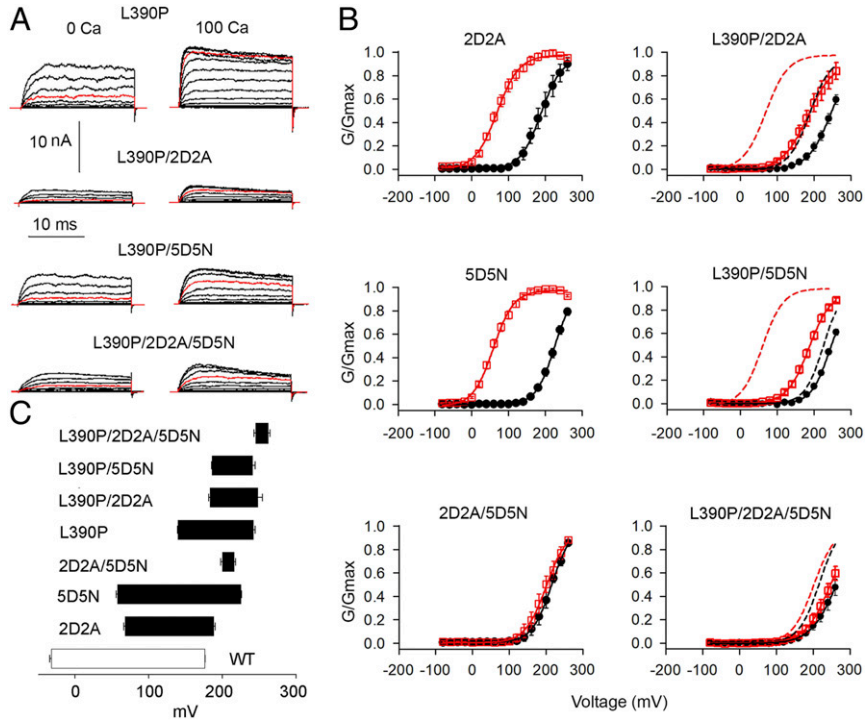

Fig. 5. Both the Ca^{2+} bowl and RCK1 Ca^{2+}-binding sites require an intact αB helix for effective Ca^{2+} activation. (*A*) Current recordings from the indicated channels. Red traces are currents at 200 mV. Voltage pulses were from −80 to 260 mV with 20-mV increments. 2D2A (D362A/D367A) disrupts the RCK1 Ca^{2+}-binding site, and 5D5N (D[898-902]A) disrupts the Ca^{2+}-bowl–binding site (7). (*B*) G/G_{max} vs. V plots in 0 Ca^{2+} (black lines through black filled circles) and 100 μM Ca^{2+} (red lines through red filled circles). Dashed lines are Boltzmann fits for WT channels and continuous lines for mutated channels. Additional data are in *SI Appendix*, Fig. S3, with Boltzmann fit parameters, SEMs, and *P* values in *SI Appendix*, Table S3. (*C*) $V_{1/2}$-Ca^{2+} bar plots, where the right end of each bar indicates 0 μM Ca^{2+} and the left end 100 μM Ca^{2+}, as mean and SEM. $n \geq 4$.

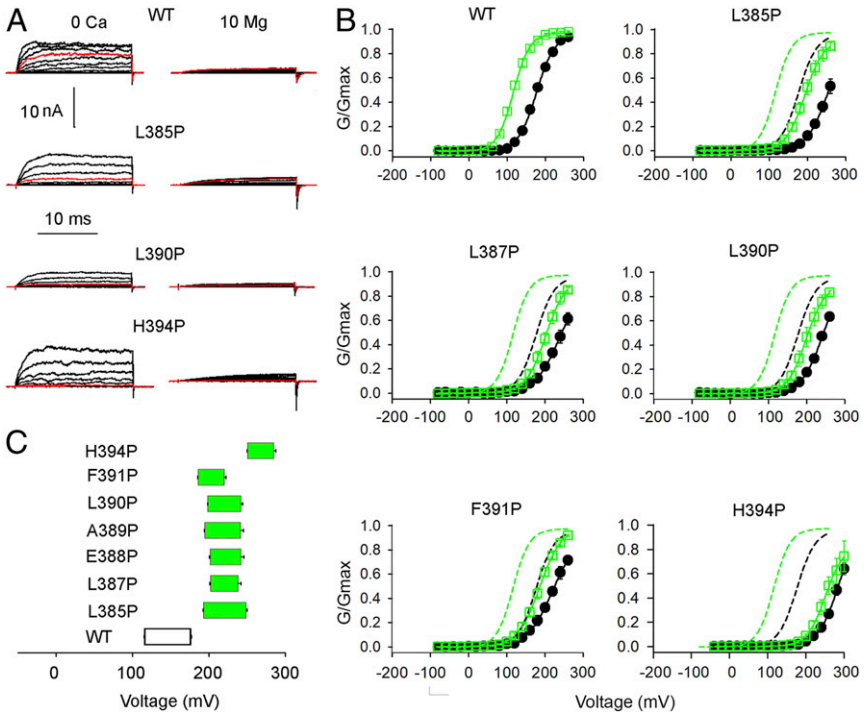

Fig. 6. Proline mutations of the αB helix reduce Mg^{2+} activation by an average of 29%. (*A*) Current recordings for the indicated channels. Red traces are currents at 200 mV. Voltage pulses were from −80 to 260 mV with 20-mV increments, except for H394P where the holding potential was −80 mV and voltage pulses were from −40 to 300 mV. (*B*) G/G_{max} vs. V plots for 0 Mg^{2+} (black lines through black filled circles) and 10 mM Mg^{2+} (green lines through open green squares). Dashed lines are Boltzmann fits for WT channels and continuous lines are Boltzmann fits for mutated channels. Additional data are in *SI Appendix*, Fig. S4. Boltzmann fit parameters, SEMs, and *P* values are in *SI Appendix*, Table S4. (*C*) $V_{1/2}$-Mg^{2+} bar plots, where the right end of each bar indicates 0 Mg^{2+} and the left end 10 mM Mg^{2+}. $n \geq 4$.

Increasing Ca^{2+} 100-Fold for Channels with Disrupted αB Helices Does Not Restore High-Affinity Ca^{2+} Sensitivity. To explore whether the proline substitutions in the αB helix decreased the Ca^{2+} activation by decreasing the effective occupancy at the high-affinity Ca^{2+}-binding sites, we increased Ca^{2+} from 100 μM to 10 mM to see if the 100-fold increase in Ca^{2+} would restore the reduced Ca^{2+}-induced left shift for αB helix-mutated channels to that of WT channels. Results are shown in Fig. 7 and *SI Appendix*, Fig. S5 and Table S2. For αB helix-mutated channels, $\Delta V_{1/2\ 0\rightarrow 100\ \mu M\ Ca}$ is plotted as black bars, and $\Delta V_{1/2\ 100\ \mu M\ \rightarrow 10\ mM\ Ca}$ is plotted as yellow bars, and, for comparison to WT channels, plotted as a white bar (Fig. 7*B*). To determine whether the 100-fold increase

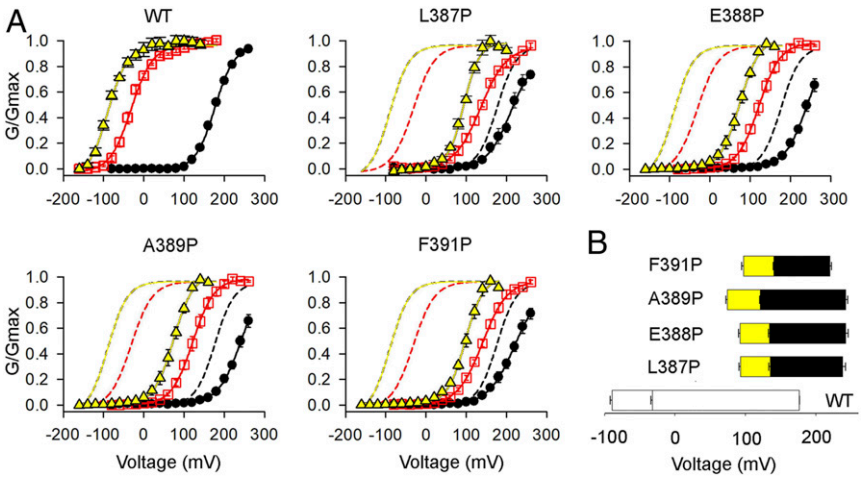

Fig. 7. The reduction in Ca^{2+} sensitivity resulting from proline mutations of the αB helix is not reversed by increasing Ca^{2+} 100-fold to 10 mM, suggesting that the reduced sensitivity is due to Ca^{2+} activation pathway dysfunction, rather than to a reduction in high-affinity Ca^{2+} binding. (*A*) G/G_{max}-V plots for the indicated channels in 0 Ca^{2+} (black lines through filled black symbols); 100 μM Ca^{2+} (red lines through red open squares); and 10 mM Ca^{2+} (yellow lines through yellow filled triangles). Dashed lines are Boltzmann fits for WT channels, and continuous lines are Boltzmann fits for mutated channels. Additional data are in *SI Appendix*, Fig. S5. Boltzmann fit parameters, SEMs, and *P* values are in *SI Appendix*, Table S2. (*B*) V-Ca^{2+} bar plots for $V_{1/2}$ in 0 μM Ca^{2+} (right end of bar), 10 mM Ca^{2+} (left end of bar), and 100 μM Ca^{2+} (line dividing each bar). $n \geq 4$.

in Ca^{2+} restores activity at the high-affinity Ca^{2+} sites, it is first necessary to know what the 100-fold increase in Ca^{2+} would do at the low-affinity Mg^{2+} site. Previous studies have shown that the low-affinity Mg^{2+} site is equally activated by 10 mM Ca^{2+} or 10 mM Mg^{2+} (7, 20, 29, 51). Consequently, the effect of changing from 0 to 10 mM Mg^{2+} on $\Delta V_{1/2}$ (Fig. 6) can be used as a measure of the expected effect of changing from 100 μM to 10 mM Ca^{2+} on the low-affinity Mg^{2+} site.

The $\Delta V_{1/2\ 100\ \mu M\ \rightarrow 10\ mM\ Ca}$ for the four examined αB helix mutations in Fig. 7 was 46.8 ± 3.2 mV (yellow bars) (data from *SI Appendix*, Table S2). This was not significantly different (P = 0.14, paired t test) from the $\Delta V_{1/2\ 0\ \rightarrow 10\ mM\ Mg}$ of 39.5 ± 3.1 mV for the same four αB helix mutations (Fig. 6*C*, green bars, data from *SI Appendix*, Table S4). Hence, this comparison suggests that increasing Ca^{2+} 100-fold in Fig. 7 increased activation through the low-affinity Mg^{2+} sites with negligible effect on the high-affinity Ca^{2+} sites. These observations would be expected if proline mutations to the αB helix decrease Ca^{2+} activation by disrupting a transduction pathway involving the αB helix, rather than by decreasing the affinity of the Ca^{2+} sensors.

Discussion

The αB Helix/VSD Interface Is Required for Effective Voltage and Ca^{2+} Activation of BK Channels. Functional studies have suggested that voltage and Ca^{2+} sensors of BK channels interact, as summarized in the Introduction (6, 14, 16, 30, 32, 41, 42, 44, 45), and that the AC (N-lobe) region of the CTD is involved (27, 52). Structural studies have identified a potential structural pathway to couple Ca^{2+} sensors in the CTD with voltage sensors in the TMD (17, 18, 33). This pathway includes protein interface interaction (*Results*) formed between the αB helices at the top of the N-lobes of the CTD and the cytoplasmic surfaces of the S4–S5 linkers/VSDs (Fig. 1). If this pathway contributes, then disruption of αB helices at the interfaces would be expected to alter both voltage and Ca^{2+} activation (Fig. 1 *A* and *B*).

We explored this possibility by creating an α-subunit of the tetrameric BK channel that has a proline substitution L390P in the αB helix, with the idea that the proline substitution would disrupt the αB helix, which in turn would alter the interface between the αB helix and S4–S5 linker/VSD. Voltage activation was found to be decreased for channels formed from the L390P subunits compared to WT channels, as indicated by 66-mV right shifts in the G-V curves (Fig. 2). The decreased voltage activation arose from a decrease in the coupling between voltage sensors and gate (Fig. 4), suggesting that the αB helix is required for effective coupling. The L390P channels also had a 49% reduction in Ca^{2+} sensitivity, as indicated by a 49% decrease in the left shift of the G-V curves induced by increasing Ca^{2+} from 0 to 100 μM (Fig. 2 and *SI Appendix*, Fig. S2 and Table S2). Both the Ca^{2+} bowl and RCK1 Ca^{2+} site were found to contribute to Ca^{2+}sensitivity in WT channels, as previously observed (7, 49). The L390P mutation then reduced the contribution from both of these sites (Fig. 5 and *SI Appendix*, Fig. S3 and Table S3), suggesting that the αB helix may form a common element in an activation pathway used by the two types of high-affinity Ca^{2+} sites.

Superposition of crystal structures of WT and mutated CTD showed that the proline mutation L390P near the middle of the αB helix (L390P) flattened the first turn of the αB helix without significant changes to other parts of the CTD (Fig. 1). Thus, the structural effects of L390P were confined to the αB helix. The altered channel function induced by the L390P mutation would then arise from altered action at the interface formed between the αB helix and the S4–S5 linker/VSD, as the remaining structure of the CTD remained unchanged and there were no other altered interface contacts with the αB helix. Single proline mutations at four other examined sites on the αB helix away from its ends gave results similar to L390P, decreasing both voltage and Ca^{2+} activation (Fig. 2 and *SI Appendix*, Fig. S2 and Table S2). Proline mutations at either end of the αB helix still decreased voltage activation, but had less of an effect on Ca^{2+} activation.

Increasing Ca^{2+} 100-fold to 10 mM did not restore Ca^{2+} sensitivity after proline mutations in the αB helix, indicating that the decrease in Ca^{2+} sensitivity was unlikely to arise from a decrease in rates for Ca^{2+} binding at the high-affinity Ca^{2+}-binding sites, consistent with structural changes from the L390P mutation of the αB helix being local to the αB helix rather than extending to the Ca^{2+}-binding sites.

Ten millimolar Mg^{2+} activated BK channels with a −60 mV shift in the G-V curves, which was decreased by αB helix mutations (Fig. 6 and *SI Appendix*, Table S4). Mg^{2+} is coordinated between E374 and E399 on top of the N-lobe and N172 and other residues on the VSD (17, 41, 53). The Mg^{2+}-coordinating site E399 on the CTD (7, 21, 54) occurs a few residues after the αB helix (Fig. 1 *C* and *D*). Consequently, altering the αB helix S4–S5 linker/VSD interface may change the spacing between the Mg^{2+}-coordinating sites on the CTD and VSD, which could alter the effectiveness of Mg^{2+} action.

Sharing of Potential Voltage and Ca^{2+} Activation Pathways of BK Channels. Previous functional observations summarized in the Introduction suggest that voltage and Ca^{2+} activation interact. Structural observations (17, 18, 33) and measurements of protein interation interfaces (*Results*) indicate that the αB helices on top of the Ca^{2+}-sensing CTD form interfaces with the S4–S5 linkers/VSDs. The interface area increases with Ca^{2+} binding and elevation of the αB helices (*SI Appendix*, Fig. S1). These observations, when taken together with our findings that a mutation-induced structural change localized to the αB helix reduced both voltage and Ca^{2+} activation, suggest that the αB helix/VSD interface contributes to both voltage and Ca^{2+} activation.

Potential voltage and Ca^{2+} activation pathways are contained within the schematic in Fig. 8 (Introduction and refs. 17, 18). TMD voltage activation would be the following: V → VSD → S5 → S6 → pore gate. αB helix-dependent voltage activation would be the following: V → VSD → αB helix → N-lobe → C-linker → S6 → pore gate. C-linker–dependent Ca^{2+} activation would be the following: Ca^{2+} → CTD → N-lobe → C-linker → S6 → pore gate. αB helix-dependent Ca^{2+} activation would be the following: Ca^{2+} → CTD → N-lobe → αB helix → VSD → S5 → S6 → pore gate.

In Fig. 8 it can be seen that the αB helix/VSD interface provides a cross-over point for voltage activation to use part of the C-linker Ca^{2+}-activation pathway in addition to using the TMD

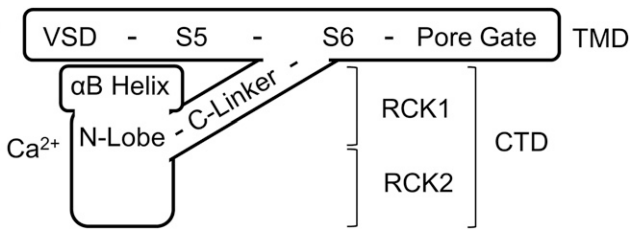

Fig. 8. Schematic diagram that includes potential voltage and Ca^{2+} activation pathways. One subunit of the BK channel is shown. In the physical channel, the αB helix is beneath the VSD and S4–S5 linker of an adjacent subunit in a swapped configuration (17). TMD voltage activation would be the following: V → VSD → S5 → S6 → pore gate. αB helix-dependent voltage activation would be the following: V → VSD → αB helix → N-lobe → C-linker → S6 → pore gate. The C-linker–dependent Ca^{2+} activation would be the following: Ca^{2+} → CTD → N-lobe → C-linker → S6 → pore gate. αB helix-dependent Ca^{2+} activation would be the following: Ca^{2+} → CTD → N-lobe → αB helix → VSD → S5 → S6 → pore gate.

voltage-activation pathway. It can also be seen that the same αB helix/VSD interface provides a cross-over point for Ca^{2+} activation to use part of the TMD voltage-activation pathway in addition to using the C-linker–dependent Ca^{2+}-activation pathway. The relative contributions of these four potential gating pathways to voltage and Ca^{2+} activation has not yet been established and is likely to change with both voltage and Ca^{2+} because both would be expected to alter the action at the αB helix/voltage sensor interface.

An extended discussion of potential voltage and Ca^{2+} activation pathways— including evidence for their contributions to gating, expected push–pull interactions between pathways (32), and their contributions to a passive spring associated with voltage gating in the absence of Ca^{2+} that has been proposed to arise from the C-linker–gating ring complex (40)—is presented in the *SI Appendix*.

Conclusion. Our experiments show that an interface formed between the αB helices at the top of the CTD and the bottom of the VSD including the S4–S5 linker is likely to play a critical role in both voltage and Ca^{2+} activation of BK channels. This αB helix/voltage sensor domain interface could couple voltage and Ca^{2+} transduction pathways, allowing voltage and Ca^{2+} to activate through both independent pathways and pathways with some shared components.

Materials and Methods

Structure Determination of Human BK CTD L390P Mutant. We determined the crystal structure of the L390P mutant by molecular replacement using the human BK CTD (Protein Data Bank [PDB] ID 3MT5) with a deletion of the αB helix (residues 384 to 394) as a search model. The αB helix harboring the L390P mutation was built near the end of structural refinement to reduce model bias from molecular replacement. The final model was refined to a resolution of 2.0 Å with R_{work}/R_{free} = 20.3%/22.5%.

Electrophysiology Recording. Site-directed mutagenesis and PCR were used to make the constructs from the mbr5 splice of variant of mSlo1 (3). Complementary RNA was synthesized and injected into *Xenopus laevis* oocytes for channel expression. Inside-out patch clamp recording (32) was used to record ionic currents and gating currents. For ionic currents, the pipette (external) solution contained the following (mM): 150 KCl, 2 $MgCl_2$, 5 2-[(2-Hydroxy-1,1-bis(hydroxymethyl)ethyl)amino]ethanesulfonic acid (TES) buffer. The 0 Ca^{2+} internal solution contained the following (mM): 150 KCl, 1 Ethylene glycol-bis(2-aminoethylether)-*N*,*N*,*N*′,*N*′-tetraacetic acid (EGTA), 1 *N*-(2-Hydroxyethyl)ethylenediamine-*N*,*N*′,*N*′-triacetic acid (HEDTA), and 5 TES, pH 7.0. The 100-μM internal Ca^{2+} solution contained (mM): 150 KCl, 0.1 $CaCl_2$, 5 TES, pH 7.0. The 10 mM internal Ca^{2+} solution contained the following (mM): 150 KCl, 10 $CaCl_2$, 5 TES, pH 7.0. The 10-mM internal Mg^{2+} solution contained (mM): 150 KCl, 10 mM $MgCl_2$, 1 EGTA, 5 TES, pH 7.0. Experiments were at 22 °C to 24 °C. Error bars are SEM.

Additional information on materials and methods is provided in *SI Appendix*.

Data Availability. The crystal structure coordinates of the human BK CTD with the L390P mutation are available at PDB ID 6V5A.

ACKNOWLEDGMENTS. This work was supported by NIH Grants R01-GM114694 (to L.S. and K.L.M.) and R01-HL142301 (to J.C.).

1. J. N. Barrett, K. L. Magleby, B. S. Pallotta, Properties of single calcium-activated potassium channels in cultured rat muscle. *J. Physiol.* **331**, 211–230 (1982).
2. E. Moczydlowski, R. Latorre, Gating kinetics of Ca^{2+}-activated K^+ channels from rat muscle incorporated into planar lipid bilayers. Evidence for two voltage-dependent Ca^{2+} binding reactions. *J. Gen. Physiol.* **82**, 511–542 (1983).
3. A. Butler, S. Tsunoda, D. P. McCobb, A. Wei, L. Salkoff, mSlo, a complex mouse gene encoding "maxi" calcium-activated potassium channels. *Science* **261**, 221–224 (1993).
4. M. Schreiber, L. Salkoff, A novel calcium-sensing domain in the BK channel. *Biophys. J.* **73**, 1355–1363 (1997).
5. B. S. Rothberg, K. L. Magleby, Voltage and Ca^{2+} activation of single large-conductance Ca^{2+}-activated K^+ channels described by a two-tiered allosteric gating mechanism. *J. Gen. Physiol.* **116**, 75–99 (2000).
6. F. T. Horrigan, R. W. Aldrich, Coupling between voltage sensor activation, Ca^{2+} binding and channel opening in large conductance (BK) potassium channels. *J. Gen. Physiol.* **120**, 267–305 (2002).
7. X. M. Xia, X. Zeng, C. J. Lingle, Multiple regulatory sites in large-conductance calcium-activated potassium channels. *Nature* **418**, 880–884 (2002).
8. L. Bao, A. M. Rapin, E. C. Holmstrand, D. H. Cox, Elimination of the BK(Ca) channel's high-affinity $Ca^{(2+)}$ sensitivity. *J. Gen. Physiol.* **120**, 173–189 (2002).
9. U. S. Lee, J. Shi, J. Cui, Modulation of BK channel gating by the ß2 subunit involves both membrane-spanning and cytoplasmic domains of Slo1. *J. Neurosci.* **30**, 16170–16179 (2010).
10. Y. Wu, Y. Yang, S. Ye, Y. Jiang, Structure of the gating ring from the human large-conductance $Ca^{(2+)}$-gated $K^{(+)}$ channel. *Nature* **466**, 393–397 (2010).
11. T. Hoshi, A. Pantazis, R. Olcese, Transduction of voltage and Ca^{2+} signals by Slo1 BK channels. *Physiology (Bethesda)* **28**, 172–189 (2013).
12. Y. Geng, K. L. Magleby, Single-channel kinetics of BK (Slo1) channels. *Front. Physiol.* **5**, 532 (2015).
13. H. Yang, G. Zhang, J. Cui, BK channels: Multiple sensors, one activation gate. *Front. Physiol.* **6**, 29 (2015).
14. A. Pantazis, R. Olcese, Biophysics of BK channel gating. *Int. Rev. Neurobiol.* **128**, 1–49 (2016).
15. R. Latorre *et al*., Molecular determinants of BK channel functional diversity and functioning. *Physiol. Rev.* **97**, 39–87 (2017).
16. Y. Zhou, H. Yang, J. Cui, C. J. Lingle, Threading the biophysics of mammalian Slo1 channels onto structures of an invertebrate Slo1 channel. *J. Gen. Physiol.* **149**, 985–1007 (2017).
17. X. Tao, R. K. Hite, R. MacKinnon, Cryo-EM structure of the open high-conductance Ca^{2+}-activated K^+ channel. *Nature* **541**, 46–51 (2017).
18. R. K. Hite, X. Tao, R. MacKinnon, Structural basis for gating the high-conductance Ca^{2+}-activated K^+ channel. *Nature* **541**, 52–57 (2017).
19. X. Tao, R. MacKinnon, Molecular structures of the human Slo1 K^+ channel in complex with β4. *eLife* **8**, e51409 (2019).
20. X. Zhang, C. R. Solaro, C. J. Lingle, Allosteric regulation of BK channel gating by Ca(2+) and Mg(2+) through a nonselective, low affinity divalent cation site. *J. Gen. Physiol.* **118**, 607–636 (2001).
21. J. Yang *et al*., Interaction between residues in the Mg^{2+}-binding site regulates BK channel activation. *J. Gen. Physiol.* **141**, 217–228 (2013).
22. R. Brenner *et al*., Vasoregulation by the beta1 subunit of the calcium-activated potassium channel. *Nature* **407**, 870–876 (2000).
23. R. Robitaille, M. L. Garcia, G. J. Kaczorowski, M. P. Charlton, Functional colocalization of calcium and calcium-gated potassium channels in control of transmitter release. *Neuron* **11**, 645–655 (1993).
24. N. Gu, K. Vervaeke, J. F. Storm, BK potassium channels facilitate high-frequency firing and cause early spike frequency adaptation in rat CA1 hippocampal pyramidal cells. *J. Physiol.* **580**, 859–882 (2007).
25. J. D. Holtzclaw, P. R. Grimm, S. C. Sansom, Role of BK channels in hypertension and potassium secretion. *Curr. Opin. Nephrol. Hypertens.* **20**, 512–517 (2011).
26. B. Wang, B. S. Rothberg, R. Brenner, Mechanism of increased BK channel activation from a channel mutation that causes epilepsy. *J. Gen. Physiol.* **133**, 283–294 (2009).
27. J. Yang *et al*., An epilepsy/dyskinesia-associated mutation enhances BK channel activation by potentiating Ca^{2+} sensing. *Neuron* **66**, 871–883 (2010).
28. H. Jiao *et al*., Genome wide association study identifies KCNMA1 contributing to human obesity. *BMC Med. Genomics* **4**, 51 (2011).
29. J. Shi, J. Cui, Intracellular Mg(2+) enhances the function of BK-type Ca(2+)-activated K(+) channels. *J. Gen. Physiol.* **118**, 589–606 (2001).
30. H. Yang *et al*., Activation of Slo1 BK channels by Mg^{2+} coordinated between the voltage sensor and RCK1 domains. *Nat. Struct. Mol. Biol.* **15**, 1152–1159 (2008).
31. G. Budelli, Y. Geng, A. Butler, K. L. Magleby, L. Salkoff, Properties of Slo1 K^+ channels with and without the gating ring. *Proc. Natl. Acad. Sci. U.S.A.* **110**, 16657–16662 (2013).
32. G. Zhang *et al*., Deletion of cytosolic gating ring decreases gate and voltage sensor coupling in BK channels. *J. Gen. Physiol.* **149**, 373–387 (2017).
33. P. Yuan, M. D. Leonetti, Y. Hsiung, R. MacKinnon, Open structure of the Ca^{2+} gating ring in the high-conductance Ca^{2+}-activated K^+ channel. *Nature* **481**, 94–97 (2011).
34. O. M. Koval, Y. Fan, B. S. Rothberg, A role for the S0 transmembrane segment in voltage-dependent gating of BK channels. *J. Gen. Physiol.* **129**, 209–220 (2007).
35. Z. Jia, M. Yazdani, G. Zhang, J. Cui, J. Chen, Hydrophobic gating in BK channels. *Nat. Commun.* **9**, 3408 (2018).
36. X. Chen, J. Yan, R. W. Aldrich, BK channel opening involves side-chain reorientation of multiple deep-pore residues. *Proc. Natl. Acad. Sci. U.S.A.* **111**, E79–E88 (2014).
37. X. H. Zeng, X. M. Xia, C. J. Lingle, Divalent cation sensitivity of BK channel activation supports the existence of three distinct binding sites. *J. Gen. Physiol.* **125**, 273–286 (2005).
38. Z. Ma, X. J. Lou, F. T. Horrigan, Role of charged residues in the S1-S4 voltage sensor of BK channels. *J. Gen. Physiol.* **127**, 309–328 (2006).
39. A. R. Pico, "*RCK domain model of calcium activation in BK channels," PhD thesis, Rockefeller University, New York* (2003).
40. X. Niu, X. Qian, K. L. Magleby, Linker-gating ring complex as passive spring and Ca(2+)-dependent machine for a voltage- and Ca(2+)-activated potassium channel. *Neuron* **42**, 745–756 (2004).
41. U. S. Lee, J. Cui, BK channel activation: Structural and functional insights. *Trends Neurosci.* **33**, 415–423 (2010).
42. T. B. Sweet, D. H. Cox, Measurements of the BKCa channel's high-affinity Ca^{2+} binding constants: Effects of membrane voltage. *J. Gen. Physiol.* **132**, 491–505 (2008).
43. N. Savalli, A. Pantazis, T. Yusifov, D. Sigg, R. Olcese, The contribution of RCK domains to human BK channel allosteric activation. *J. Biol. Chem.* **287**, 21741–21750 (2012).

44. Y. Lorenzo-Ceballos, W. Carrasquel-Ursulaez, K. Castillo, O. Alvarez, R. Latorre, Calcium-driven regulation of voltage-sensing domains in BK channels. *eLife* **8**, e44934 (2019).
45. P. Miranda, M. Holmgren, T. Giraldez, Voltage-dependent dynamics of the BK channel cytosolic gating ring are coupled to the membrane-embedded voltage sensor. *eLife* **7**, e40664 (2018).
46. F. T. Horrigan, J. Cui, R. W. Aldrich, Allosteric voltage gating of potassium channels I. Mslo ionic currents in the absence of Ca(2+). *J. Gen. Physiol.* **114**, 277–304 (1999).
47. J. Cui, D. H. Cox, R. W. Aldrich, Intrinsic voltage dependence and Ca^{2+} regulation of mslo large conductance Ca-activated K^+ channels. *J. Gen. Physiol.* **109**, 647–673 (1997).
48. R. Guan *et al*., Allosteric-activation mechanism of BK channel gating ring triggered by calcium ions. *PLoS One* **12**, e0182067 (2017).
49. A. S. Kshatri, A. J. Gonzalez-Hernandez, T. Giraldez, Functional validation of Ca^{2+}-binding residues from the crystal structure of the BK ion channel. *Biochim. Biophys. Acta Biomembr.* **1860**, 943–952 (2018).
50. Q. Li *et al*., Molecular determinants of Ca^{2+} sensitivity at the intersubunit interface of the BK channel gating ring. *Sci. Rep.* **8**, 509 (2018).
51. L. Hu, H. Yang, J. Shi, J. Cui, Effects of multiple metal binding sites on calcium and magnesium-dependent activation of BK channels. *J. Gen. Physiol.* **127**, 35–49 (2006).
52. G. Krishnamoorthy, J. Shi, D. Sept, J. Cui, The NH_2 terminus of RCK1 domain regulates Ca^{2+}-dependent BK(Ca) channel gating. *J. Gen. Physiol.* **126**, 227–241 (2005).
53. H. Yang *et al*., Mg^{2+} mediates interaction between the voltage sensor and cytosolic domain to activate BK channels. *Proc. Natl. Acad. Sci. U.S.A.* **104**, 18270–18275 (2007).
54. J. Shi *et al*., Mechanism of magnesium activation of calcium-activated potassium channels. *Nature* **418**, 876–880 (2002).
55. P. Yuan, M. D. Leonetti, A. R. Pico, Y. Hsiung, R. MacKinnon, Structure of the human BK channel Ca^{2+}-activation apparatus at 3.0 A resolution. *Science* **329**, 182–186 (2010).